APSB
Acta Pharmaceutica Sinica B
2020
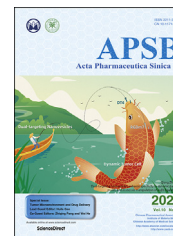
ORIGINAL ARTICLE

Dual-targeting nanovesicles enhance specificity to dynamic tumor cells *in vitro* and *in vivo via* manipulation of $\alpha v\beta 3$-ligand binding

Yang Song[a,†], Xiangfu Guo[a,†], Jijun Fu[b], Bing He[a], Xueqing Wang[a], Wenbing Dai[a], Hua Zhang[a], Qiang Zhang[a,*]

[a]Beijing Key Laboratory of Molecular Pharmaceutics and New Drug Delivery Systems, State Key Laboratory of Natural and Biomimetic Drugs, School of Pharmaceutical Sciences, Peking University, Beijing 100191, China
[b]Guangzhou Medical University, School of Pharmaceutical Sciences, Guangzhou 511436, China

Abstract   The dynamic or flowing tumor cells just as leukemia cells and circulating tumor cells face a microenvironment difference from the solid tumors, and the related targeting nanomedicines are rarely reported. The existence of fluidic shear stress in blood circulation seems not favorable for the binding of ligand modified nanodrugs with their target receptor. Namely, the binding feature is very essential in this case. Herein, we utilized HSPC, PEG-DSPE, cholesterol and two $\alpha v\beta 3$ ligands (RGDm7 and DT4) with different binding rates to build dual-targeting nanovesicles, in an effort to achieve a "fast-binding/slow-unbinding" function. It was demonstrated that the dual-targeting nanovesicles actualized efficient cellular uptake and antitumor effect *in vitro* both for static and dynamic tumor cells. Besides, the potency of the dual-targeting vesicles for flowing tumor cells was better than that for static tumor cells. Then, a tumor metastasis mice model and a leukemia mice model were established to detect the killing ability of the drug-loaded dual-targeting vesicles to dynamic tumor cells *in vivo*. The therapy efficacy of the dual-targeting system was higher than other controls including single-targeting ones. Generally, it seems possible to strengthen drug-targeting to dynamic tumor cells *via* the control of ligand−receptor interaction.

1. Introduction

A considerable part of tumor cells in human body are scattered in flowing blood system, including leukemia cells and circulating tumor cells (CTCs)[1]. Tumor cells under flowing condition do great harm to human health. Leukemia accounts for nearly 10% of all new cancer cases in the US and Canada[2]. Besides, CTCs can cause poor prognosis and tumor metastasis[3], while metastasis increases morbidity and mortality of cancer[4]. As widely known, delivering nanodrugs to solid tumors can be improved by enhanced permeability and retention (EPR) effect[5]. However, there are no such options for the dynamic tumor cells in the circulation due to the lack of the EPR effect.

In the past years, the nanopreparations against dynamic tumor cells mainly focus on leukemia and based on lipid vesicles due to the biocompatibility[6]. For example, arsenic trioxide-liposomes, CD123/CD33 dual-antibody modified lipid vesicles, as well as dual-action CXCR4-targeting liposomes have been reported for leukemia treatment[7−9]. Recently, a liposomal cytarabine/daunorubicin formulation (CPX-351) for acute myeloid leukemia was approved by the U.S. Food and Drug Administration (FDA)[10]. Interestingly, the improved efficacy of CPX-351 is a result of enhanced drug level in bone marrow instead of targeting to leukemia cells flowing in bloodstream[11]. CPX-351 achieves a longer pharmacokinetic exposures of two drugs compared with conventional chemotherapy[12]. Generally, the dynamic tumor cells are common actually, but the investigation on related nanomedicines is very rare.

The integrin $\alpha v\beta 3$ is widely used as a target for tumor diagnosis and therapy because it is overexpressed in various tumor cells[13]. Arginine-glycine-aspartic acid (RGD) can recognize the $\alpha v\beta 3$, so a series of RGD were synthesized for targeting tumor cells[14−16]. A new bicyclic RGD, cRGD-ACP-K (recorded as RGDm7), was reported with greater affinity than traditional RGD peptides and was used as a positron emission computed tomography (PET) radiotracers for tumor imaging[17]. On the other hand, thyroid hormone is a series of molecules regulating various living activities. The major active form of thyroid hormone, 3,3′,5-triiodothyronine (T3), is converted from thyroxine (T4), which is secreted by the thyroid gland[18]. T4 has a significant binding activity with $\alpha v\beta 3$, yet it can promote tumor cell proliferation and tumor angiogenesis[19,20]. As an enantiomer of T4, D-thyroxine (DT4) has a much lower biological activity, but it can bind to the nuclear T3-receptors with an almost equal affinity as T3[21,22]. Notably, there is no report on binding ability of DT4 with $\alpha v\beta 3$.

Herein, we studied the binding affinity of RGDm7 and DT4 to integrin $\alpha v\beta 3$ by SPR assay. It was found that both RGDm7 and DT4 could specifically bind with $\alpha v\beta 3$, but their association/dissociation patterns were different. RGDm7 acted as a "slow-binding/slow-unbinding" ligand while DT4 showed a fast association and dissociation. The difference in their binding behavior provides a possibility to design a type of "fast-binding/slow-unbinding" delivery nanomedicines, as well as a risk of "slow-binding/fast-unbinding" mode, by decorating both RGDm7 and DT4 on the surface of lipid vesicles. Additionally, doxorubicin (DOX) is a well-established chemodrug in the field of cancer treatment, as Doxil® became the first long-circulating liposomes proved by the FDA[23].

Based on the background above, in an attempt to enhance the targeting of nanomedicines to the dynamic tumor cells, we designed and engineered a dual-targeting lipid vesicle *via* the decoration with both RGDm7 and DT4, on the basis of our finding on the binding/unbinding rate. It is expected that DT4 helps the vesicles adhere quickly to the flowing tumor cells and transfer drug to nucleus, while RGDm7 contributes to the stable binding with $\alpha v\beta 3$. We investigated endocytosis and cytotoxicity mediated by dual-targeting lipid vesicles *in vitro* both in static and flowing situation. Besides, we used tumor metastasis mice model and a novel leukemia mice model to detect the killing ability to dynamic tumor cells. The anti-tumor mechanism was also studied by cellular co-localization analyses and uptake inhibition test.

2. Materials and methods

2.1. Detection of receptor expression

Jurkat cells were resuspended in cell staining buffer at 5×10^6 cells/mL and 100 μL cell suspension was transferred into each EP tube. Fc receptors were blocked with 5 μL Human TruStain FcX™ per 100 μL of cell suspension for 5 min at room temperature. 5 μL Alexa Fluor® 647 anti-human CD51/61 antibody was added in 100 μL cell suspension and was incubated on ice in the dark for 15 min. Cells were washed 2 times with 1.9 mL cell staining buffer by centrifugation at $350 \times g$ for 5 min. Cell suspension was resuspended in 500 μL cell staining buffer and 5 μL 7-AAD viability staining solution was added to exclude dead cells. Cells were incubated on ice in the dark for 3 min and were analyzed with flow cytometry.

2.2. Detection of ligand affinity by surface plasmon resonance (SPR) assay

All SPR measurement was performed at room temperature on BIAcore® T200 (GE Healthcare, Fairfield, USA)[24]. HBS-N (10 mmol/L HEPES, 150 mmol/L NaCl, pH = 7.4) was used as the running buffer. After activating the sensor surface with a 1:1 mixture of 0.4 mol/L EDC (1-ethyl-3-(3-dimethylaminopropyl)-carbodiimide), and 0.1 mol/L NHS (N-hydroxysuccinimide), 50 μg/mL $\alpha v\beta 3$ (diluted in 10 mmol/L acetate solution, pH = 5.0) was injected for 20 min at a flow rate of 5 μL/min. Blocked the sensor surface with 1 mmol/L ethanolamine-HCl solution (pH = 8.5). PBSt (1 mmol/L KH_2PO_4, 10 mmol/L Na_2HPO_4, 137 mmol/L NaCl, 2.7 mmol/L KCl pH 7.4, 0.05% Tween20) was used as running and dilution buffer and the flow rate was kept at 5 μL/min. RGDm7 or DT4 was injected at various concentrations (C) for 60 s. After 120 s of dissociation, injected 10 mmol/L

glycine for 30 s to remove any non-covalently bounded ligands from the sensor surface. Recorded the response−time (R−−e simplified as followed reversible reaction:

$$A + B \underset{k_d}{\overset{k_a}{\rightleftharpoons}} AB$$
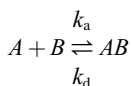
Association rate constant (k_a), dissociation rate constant (k_d) and the equilibrium dissociation constant (K_D) can be calculated by following Eqs. (1)−(4):

$$\mathrm{d}[AB] / \mathrm{d}t = k_a \cdot [A] \cdot [B] \tag{1}$$

$$-\mathrm{d}[AB] / \mathrm{d}t = k_d \cdot [AB] \tag{2}$$

$$\mathrm{d}R / \mathrm{d}t = k_a \cdot C \cdot [R_{max} - R] - k_d \cdot R \tag{3}$$

$$K_D = k_d / k_a \tag{4}$$

2.3. Synthesis and characterization of targeting lipid molecules

The targeting lipid molecules RGDm7-PEG-DSPE and DT4-PEG-DSPE were synthesized. All the synthetic methods and characterizations are shown in the Supporting Information.

2.4. Construction of lipid vesicles

Here we prepared single-targeting and dual-targeting lipid vesicles (R-LIPO, D-LIPO and RD-LIPO, where R refers to RGDm7, and D means DT4) with different ligand concentrations. No ligand modified lipid vesicles (LIPO) were also prepared as control. The percentage of targeting lipid molecules refers to the mass fraction of targeting lipid molecules in all DSPE-PEG. Lipid vesicles were composed of HSPC/CH/DSPE-PEG (3:1:1, w/w/w). Cholesterol was used to reduce the rigidity of the lipid membrane and enhance the penetration of lipid vesicles[25]. All DOX-loaded lipid vesicles (lipids:DOX = 10:1, w/w) were prepared using the lipid film hydration method. Briefly, the lipids were dissolved in chloroform and evaporated at 40 °C. The film was hydrated with 250 mmol/L ammonium sulfate solution and was heated in water bath at 55 °C. After sonication with supersonic cell disruptor JY92-2D (SCIENTZ, Ningbo, China), the liposomal suspension was distributed immediately into Sephadex G-50. Collected the filtrated suspension and adjusted the pH to 7.0−7.5. Then DOX·HCl solution was added dropwisely into the liposomal suspension under stirring in 75 °C water bath. The mixture was stirred and heated for 20 min then cooled the mixture using ice-bath.

Preparations of coumarin-6 (C6) encapsulated lipid vesicles (lipids:C6 = 1000:1, w/w) and DiR encapsulated lipid vesicles (lipids:DiR = 1000:5, w/w) were similar to that of DOX-loaded lipid vesicles. C6 or DiR was co-dissolved with lipids and the film was hydrates with distilled water, while steps for loading DOX were omitted.

2.5. Characterization of lipid vesicles

The particle size and zeta potential of lipid vesicles were analyzed by dynamic light scattering (DLS) analysis using Malvern Zetasizer Nano ZS (Malvern Instruments, Malvern, Worcestershire, UK). The morphology was observed with transmission electron microscopy JEM-200CX (JEOL, Akishima, Tokyo, Japan). The drug loading and encapsulation efficiency of DOX-loaded lipid vesicles were determined with sephadex-G50 mini-column centrifuge.

2.6. In vitro endocytosis of lipid vesicles

2.6.1. In vitro static endocytosis
Jurkat cells (5×10^5 cells/mL) were resuspend and distributed in 24-well plates. Then different C6 encapsulated lipid vesicles were added while the concentration of C6 was 50 ng/mL[26]. After incubation at 37 °C under static condition for 48 h, cells were washed with cold PBS three times and analyzed by FACS Calibur flow cytometer (Becton Dickinson, San Jose, CA, USA).

Real-time confocal was used to analyze the uptake kinetics of the lipid vesicles. Jurkat cells were adhered on a glass-bottom dish covered with Cell-Tak™ Cell and Tissue Adhesive. After the lipid vesicle suspension (containing 50 ng/mL C6) was added, confocal images were recorded continuously with Zeiss LSM880 (Carl Zeiss AG., Jena, Thuringia, Germany). Four regions of interests (ROI) from each microscopic field were selected randomly. The uptake kinetics was analyzed by Zeiss ZEN (Carl Zeiss AG., Jena, Thuringia, Germany).

2.6.2. In vitro dynamic endocytosis
We evaluated the cellular uptake ability under different flowing condition. In order to simulate the fast flow rate environment, Jurkat cells suspension (1×10^5 cells/mL) was added into a peristaltic pump pipe (the inside diameter was 1.6 mm) and flowed at a rate of 10 mL/min. The slow flow rate condition was provided by a 100 rpm shaking table. After incubated with different lipid vesicle suspension (containing 100 ng/mL C6) for 30 min, cells were washed with cold PBS three times and analyzed by FACS-Calibur flow cytometer.

2.7. In vitro efficacy of different lipid vesicles

2.7.1. In vitro efficacy against static tumor cells
The cytotoxicity of DOX-loaded lipid vesicles was evaluated by CCK-8 assay on Jurkat cells. Briefly, Jurkat cells (2×10^5 cells/mL) were distributed in 96-well plates (100 μL per well). Then cells were exposed to different lipid vesicles (the concentration calculated as DOX). After 48 h incubation, 10 μL CCK-8 was added into each well followed by a 2 h incubation. The UV absorbance at 480 nm was determined by a 96-well plate reader (Thermo Scientific, Waltham, USA).

2.7.2. In vitro efficacy against dynamic tumor cells
Jurkat cells (2×10^5 cells/mL) were resuspended by different DOX-loaded lipid vesicles diluted with RPMI 1640 and were distributed in 2 mL EP tubes. After incubating at 500 rpm for 48 h by hermomixer TS100 (Ruicheng Instrument Co., Ltd., Hangzhou, China), the cell viability was determined by CCK-8 assay.

2.8. In vivo antineoplastic therapy and biodistribution

2.8.1. Antitumor efficacy in leukemia mice models
The female NPG mice were supplied by Beijing Vitalstar Biotechnology Co., Ltd. (Beijing, China) and were fed under SPF condition. The female C57BL/6 mice and female BALB/c nu/nu mice were obtained from Peking University Health Science Center, China. All mouse studies adhered to the principles of care and use of laboratory animals and were approved by the

Institutional Animal Care and Use Committee of Peking University, China.

The NPG mice were intravenously injected with 1×10^6 Jurkat cells. At 2 h post cell infusion, different DOX-loaded lipid vesicles (4 mg/kg, calculated as DOX) were injected through the tail vein, and 11 days after cell infusion, lipid vesicles were injected again at a 2 mg/kg DOX dose. The mice were sacrificed when they are paralyzed. Survival time was evaluated and organs were harvested at 1 month for tissue section analysis. Leg bones treated with decalcifying solution and hearts were frozen and fixed on poly lysine coated glass slides. After hematoxylin-eosin (H&E) staining, morphological changes were observed by microscope. NanoSPECT/CT images were detected by NIKON digital sight DS-FI2 (NIKON Inc., Minato, Tokyo, Japan).

2.8.2. Antitumor efficacy in tumor metastasis models

To establish the lung metastatic models, the C57BL/6 mice were intravenously injected with 1×10^5 B16F10 cells and were randomly divided into two groups, an early-treatment group and a late-treatment group. The mice of early-treatment group were injected with different DOX-loaded lipid vesicles (4 mg/kg, calculated as DOX) at 2 h post-cell infusion, while at 7, 9 and 11 days post-cell infusion, the mice of late-treatment group were injected with lipid vesicles at a 2 mg/kg DOX dose each time. Lungs were harvested and the size and number of metastatic nodules on the lung surfaces were determined.

2.8.3. Biodistribution of lipid vesicles

The NPG mice were injected with 1×10^6 Jurkat cells through the tail vein. At 7 days post cell infusion, the mice were randomly divided into five groups and intravenously injected with PBS, free DiR and three different DiR-loaded lipid vesicles respectively. The dose of DiR was 1.5 μg/mouse. At 5, 12, 24 and 48 h post injection, the mice were anesthetized with 1% isoflurane in oxygen and acquired fluorescent images within the scope of 745 nm exciting light and 800 nm emission light by an *in vivo* imaging system (IVIS SPECTRUM PerkinElmer, Waltham, USA). *Ex vivo* fluorescent images of tissues were obtained at 48 h post injection. The mean fluorescence intensity of whole body and tissues was analyzed using Carestream software.

2.9. Co-localization analysis of lipid vesicles with nucleuses or lysosomes

Jurkat cells (5×10^5 cells/mL) were exposed with 10 μg/mL (calculated as DOX) different DOX-loaded lipid vesicles for 30 min. Then the lipid vesicle suspension was removed and cells were adhered on glass-bottom dishes covered with Cell-Tak™ Cell and Tissue Adhesive. After incubation with LysoTracker Green DND-26 and Heochst 33,342 for 30 min, the co-localizations between nucleuses, lysosomes and lipid vesicles were studied by CLSM.

2.10. Effect of different inhibitors on endocytosis

Jurkat cells (5×10^5 cells/mL) were resuspend and distributed in 24-well plates. After pre-incubation with inhibitors for 30 min (shown in Supporting Information Table S4), different lipid vesicles were added in the wells with a C6 concentration of 50 ng/mL and incubated for 30 min. The other steps were same as that of *in vitro* cellular uptake.

2.11. Statistical analysis

Data were expressed as mean ± standard deviation (SD). The results were analyzed by Student's *t* test. If *P* values are less than 0.05, the differences were considered as statistically significant.

3. Results

3.1. Construction and features of targeted lipid vesicles

The dual-targeting lipid vesicles were prepared with both RGDm7-PEG-DSPE and DT4-PEG-DSPE. Ligands and DSPE-PEG2000-NHS were conjugated by one step reaction (Supporting Information Scheme S1). To increase the yield of RGDm7-PEG-DSPE and DT4-PEG-DSPE, reactions were conducted under anhydrous conditions and pH was adjusted by triethylamine. Supporting Information Figs. S3 and S4 show the results of MALDI-TOF-MS and ^{1}H NMR. In the preparation process of DOX-loaded lipid vesicles, DT4 conjugated lipid vesicles were prone to coagulate in ammonium sulfate solution, so we removed the ions from the external aqueous phase as soon as lipid vesicles were sonicated.

The particle size, polydispersity index (PDI) and zeta potential of different DOX-loaded lipid vesicles are shown in Fig. 1B and Table 1. The mean sizes of all kinds of lipid vesicles were near 100 nm, which is important for lipid vesicle biodistribution and cellular uptake[27]. The PDIs were all under 0.3, which means lipid vesicles had a uniform size distribution. TEM results in Fig. 1A showed that all DOX-loaded lipid vesicles were hollow spheres. Compared with blank lipid vesicles (Supporting Information Fig. S5), DOX formed a sediment inside the lipid vesicles. Besides, the encapsulation efficiencies of DOX were all above 80% (Supporting Information Table S1). The *in vitro* release behaviors of different lipid vesicles are shown in Supporting Information Supporting Information Fig. S6. Ligand modified lipid vesicles showed a reduction in releasing rate at 24 h, probably caused by the differences of phase-transition temperature. Particle size of different lipid vesicles kept constant during 3 day blood stability test (Supporting Information Fig. S12A and S12B), while no hemolysis was found for all formulations (Fig. S12C).

Coumarin-6 (C6) was widely used as a fluorescent marker for lipid vesicle tracing. Less than 1% of C6 leaked from different C6 encapsulated lipid vesicles within 36 h in the *in vitro* leakage experiment (Supporting Information Fig. S7), suggesting that most C6 remained in lipid vesicles in the following test of cellular uptake. The particle size and PDI are shown in Supporting Information Table S2. DiR iodide was a fluorescence probe used for live imaging of small animals. The mean sizes and PDI of DiR encapsulated lipid vesicles listed in Supporting Information Table S3 met the requirements of *in vivo* distribution.

3.2. $\alpha v \beta 3$ expression and its binding/unbinding with RGDm7 and DT4

Fig. 2A shows the integrin $\alpha v \beta 3$ expression in two different cell lines. Jurkat cells highly expressed $\alpha v \beta 3$ while K562 cells did not. The latter is an $\alpha v \beta 3$ negative myeloid leukemia cell line, so it is reasonable to use it as a cell control.

We used SPR to detect real-time interaction between $\alpha v \beta 3$ and targeting molecules (RGDm7 and DT4). The binding capacity was reflected by the refractive index change of sensor surface[28]. The

A

LIPO-DOX

50R-LIPO-DOX

10D-LIPO-DOX

50R10D-LIPO-DOX

B
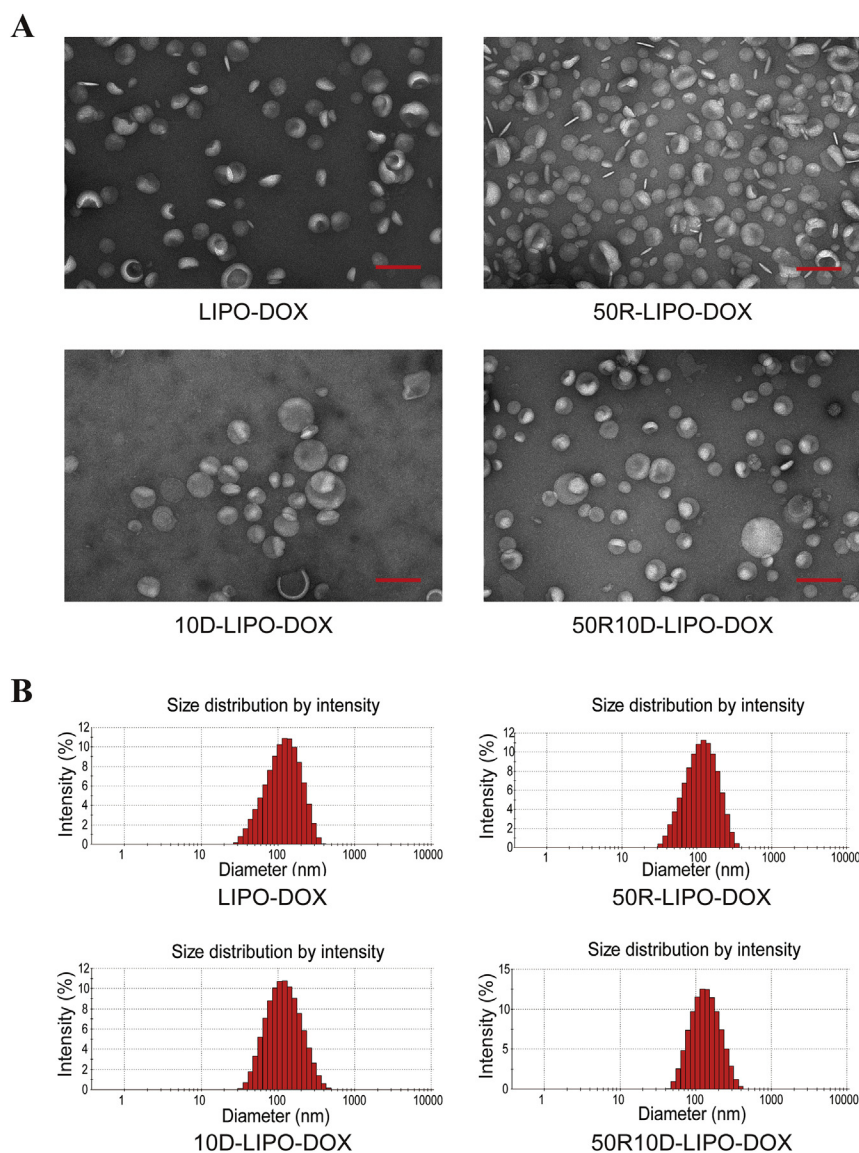
Figure 1 (A) The morphology of LIPO-DOX, 50 R-LIPO-DOX, 10D-LIPO-DOX and 50R10D-LIPO-DOX observed by TEM. Scale bars = 200 nm. (B) Particle size distributions of the lipid vesicles determined by DLS.

$\alpha v\beta 3$ was fixed on the sensor surface *via* covalent binding. RGDm7 or DT4 solution flowed over the sensor surface in the same way but these two ligands showed different binding behaviors (Fig. 2B). Interestingly, the response signal (RU) increased rapidly when DT4 was injected, while the RU of RGDm7 increased slowly. As for the dissociation process, after loading buffer was injected, the RU of DT4 decreased quickly, while it took a longer time for RGDm7. The curve fitting analysis in Fig. 2C showed that the K_D of RGDm7 was about eight times as much as that of DT4. Based on these findings, we concluded that

Table 1 The particle size, PDI and zeta potential of DOX loaded lipid vesicles.

Formulation	Size (nm)	PDI	Zeta potential (mV)
LIPO-DOX	104.4 ± 0.59	0.138 ± 0.001	−40.0 ± 0.529
50R-LIPO-DOX	99.7 ± 1.02	0.135 ± 0.002	−24.3 ± 0.651
10D-LIPO-DOX	117.2 ± 1.64	0.166 ± 0.012	−40.6 ± 0.755
50R10D-LIPO-DOX	112.4 ± 2.55	0.154 ± 0.003	−27.7 ± 0.458

Data are presented as mean ± SD, n = 3.

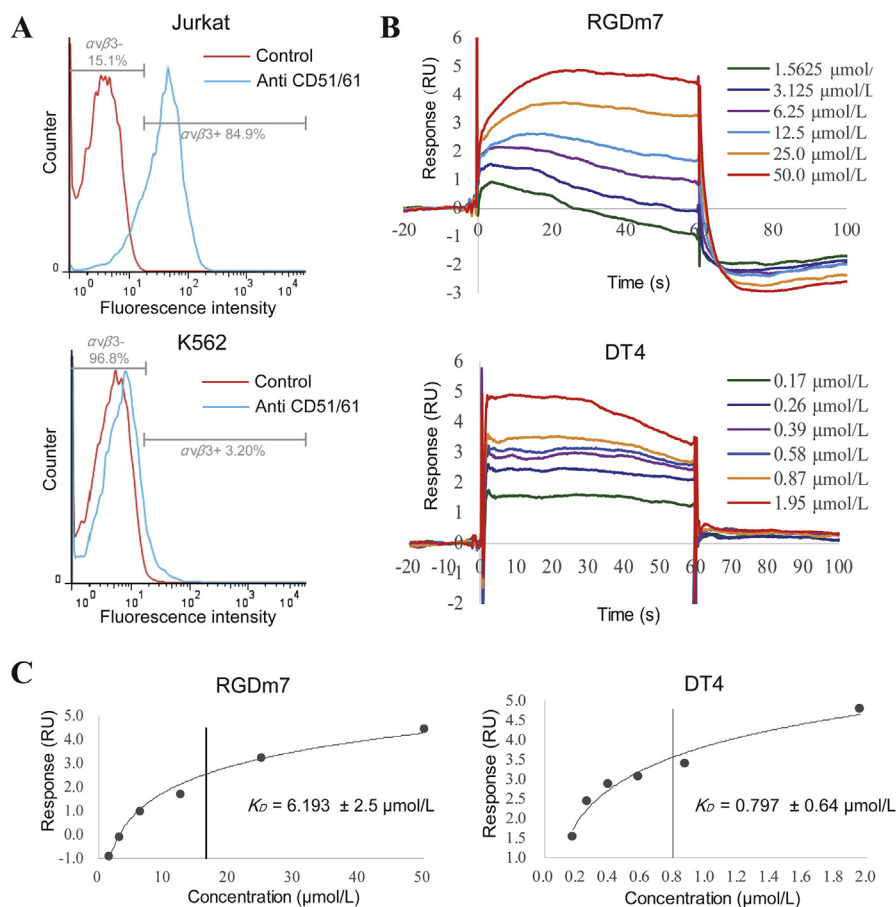**Figure 2** (A) Detection of $\alpha v\beta 3$ expressions in different cell lines by flow cytometry. Red curves represent cells incubated with antibody. Blue curves represent cells without antibody incubation. (B) Surface plasmon resonance responses to different concentrations of RGDm7 and DT4 with $\alpha v\beta 3$ during a 100-s injection. (C) Concentration−response curves of the binding signal.

RGDm7 could interact with $\alpha v\beta 3$ in a "slow-binding/slow-unbinding" pattern, while DT4 act as a "fast-binding/fast-unbinding" targeting molecule.

3.3. In vitro static and dynamic endocytosis of targeted lipid vesicles

Via flow cytometry assay, we compared the uptake capability between different lipid vesicles in Jurkat cell line under static and dynamic situations. The ligand-modified lipid vesicles included single-targeting (R-LIPO-C6, D-LIPO-C6) and dual-targeting vesicles (RD-LIPO-C6). As showed in Fig. 3A, under static situation, when the percentage of RGDm7 was 30% and 50%, the uptake of dual-targeting lipid vesicles was more than single-targeting lipid vesicles or negative control. Under flowing situation, DT4 modified lipid vesicles demonstrated the most uptake. But with the increase of flow rate, the uptake quantity decreased significantly (Fig. 3B).

The confocal microscopy demonstrated that the lipid vesicles were taken into cells instead of sticking to the cell surface (Fig. 3C). We also utilized real-time confocal microscopy to detect the uptake kinetics of different lipid vesicles in Jurkat cell lines (Fig. 3D). Understandably, dual-targeting lipid vesicles showed the most uptake at the end of observation. According to real-time confocal microscopy, DT4-LIPO exhibited faster uptake at the beginning, and soon remained a relatively constant uptake.

The dual-targeting lipid vesicles were taken up continuously and exceeded DT4 in quantity finally. This might be due to the different binding mode of RGDm7 and DT4.

3.4. In vitro efficacy of targeted lipid vesicles against static or dynamic tumor cells

The IC_{50} of Jurkat cells after treatment with different lipid vesicles (LIPO-DOX, R-LIPO-DOX, D-LIPO-DOX, RD-LIPO-DOX) under static situation is shown in Fig. 4A. Under the same concentration of RGDm7, all the dual-targeting lipid vesicles showed lower IC_{50} than R-LIPO. Under flowing situation as seen in Fig. 4B, the cell viability of Jurkat cells was the smallest in the group of 50R10D-LIPO-DOX (50 and 10 refers to 50% and 10%, respectively). As for the IC_{50} of $\alpha v\beta 3$ negative K562 cells, no significant difference was observed between negative control and targeting lipid vesicles, which related the cytotoxicity of lipid vesicles to the targeting ability of $\alpha v\beta 3$ (Fig. 4C). B16F10 cell line was used later to build tumor lung metastasis model[29], and $\alpha v\beta 3$ was reported to highly express on B16F10 cells[30]. Here, in the study with B16F10 cells, the targeting lipid vesicles had a lower IC_{50} value than negative control, while dual-targeting lipid vesicles demonstrated stronger cytotoxicity than single-targeting lipid vesicles, revealing the contribution of $\alpha v\beta 3$ to the cytotoxicity of targeting lipid vesicles (Fig. 4D). We also compared the in vitro efficacy of mixed single-targeting lipid vesicles and dual-
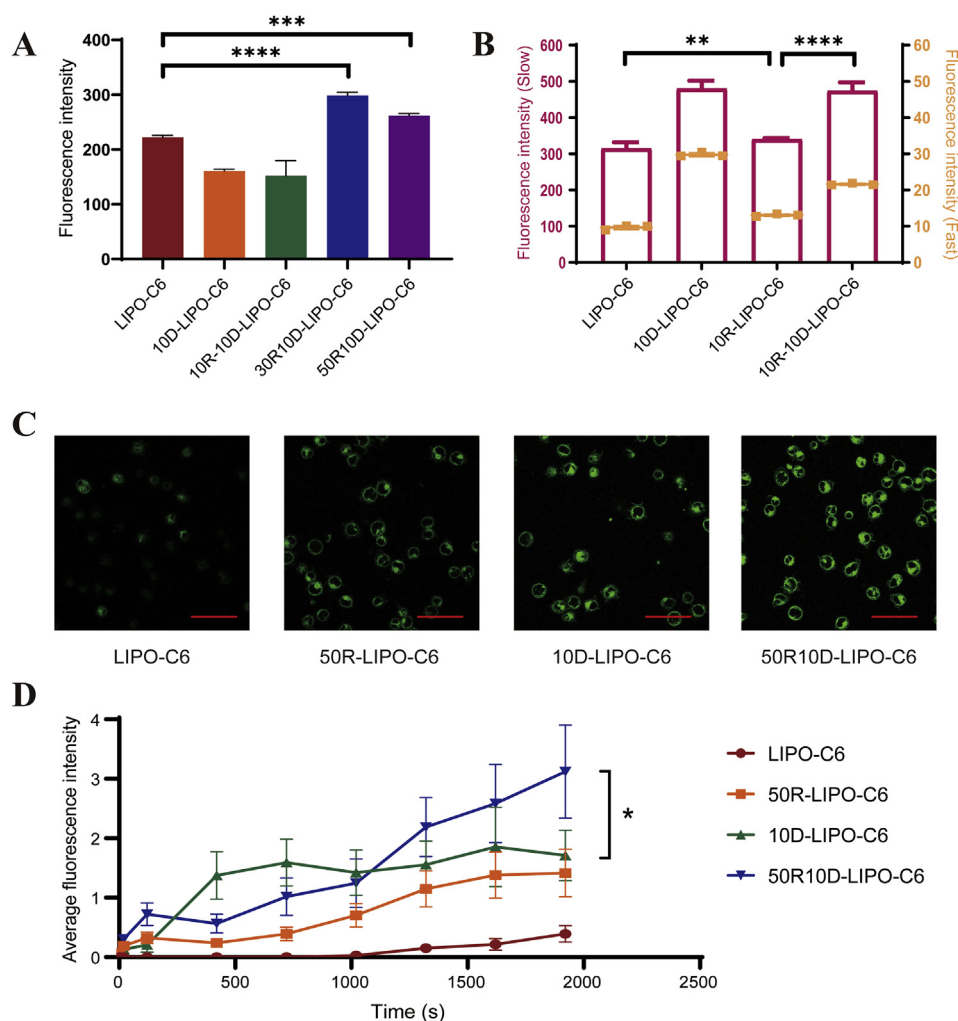
Figure 3 (A) Cellular uptake in Jurkat cells after incubation with different lipid vesicles and controls under static condition for 48 h. (B) Cellular uptake under different flowing condition. Red columns refer to fluorescence intensity of cells in slow flow rate environment and yellow subcolumns represent fluorescence intensity under fast flow rate condition. Data are represented as mean ± SD ($n = 3$), **$P < 0.01$, ***$P < 0.001$, ****$P < 0.0001$. (C) Confocal images of Jurkat cells after incubation with different lipid vesicles for 32 min. Green represents the different lipid vesicles. Scale bars are 50 μm. (D) Quantitative cellular uptake data detected by confocal microscopy. Data are represented as mean fluorescence intensity±SD ($n = 4$).

targeting ones (Supporting Information Fig. S14). The IC$_{50}$ of mixed vesicles was significantly higher than that of dual-targeting formulation, revealing that the later was better in the treatment.

3.5. In vivo antineoplastic therapy and biodistribution

3.5.1. Antitumor efficacy in leukemia mice models
50 R-LIPO-DOX, 10D-LIPO-DOX and 50R10D-LIPO-DOX were selected for further study as their higher cytotoxicity and cellular uptake. LIPO-DOX was used as negative control. To evaluate the *in vivo* therapeutic effects on leukemia mice models, lipid vesicles were injected at 2 h and 11 days after cell infusion, and major tissues were analyzed at Day 30 (Fig. 5A). It was previously reported that leukemia mice could have the limb paralysis, and the spinal metastasis of tumor cells could cause the deformation of spinal column[31,32]. Here, leukemia mice also showed hind limb paralysis during the experiment (Supporting Information Fig. S8A and S8B), and the time of paralysis might reflect the antitumor

efficacy of nanomedicines. NanoSPECT/CT study displayed spine curvature in paralyzed mice (Figs. S8C and S8D). The body weight was decreased about 10% within 15 days after lipid vesicle administration, which was taken as an index of drug systemic toxicity. The mice in the control group lost relatively less body weight, while there was no significantly difference in body weight among different lipid vesicle formulations (Fig. 5B). The median survival of mice treated with dual-targeting lipid vesicles was 5 days more than that with 10D-LIPO-DOX, and 9 days more than that with LIPO-DOX or 50 R-LIPO-DOX (Fig. 5C). A large number of tumor cells could be seen in the bone marrow cavity, the nucleocytoplasmic ratio was high and abnormal cell nuclei were visible in each group. While, there was less bone marrow necrosis in mice treated with dual-targeting lipid vesicles (Fig. 5D). Finally, the HE staining of heart tissues was also conducted to detect the cardiotoxicity (Supporting Information Fig. S13). The myocardial fiber morphology was normal and no obvious inflammation was observed in each group.
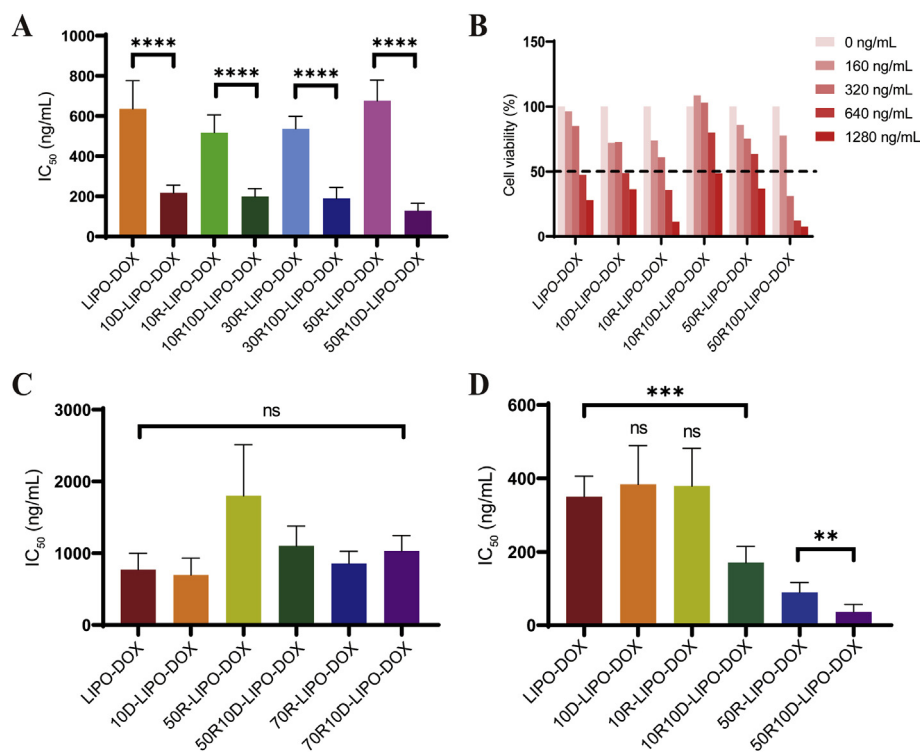
Figure 4 The IC$_{50}$ of different lipid vesicles against Jurkat cells after 48 h incubation under static situation (data are represented as mean IC$_{50}$±SD, $n = 6$) (A) or in a shaking table (data are represented as mean cell viability±SD, $n = 3$) (B) by CCK-8 assay. The IC$_{50}$ of different lipid vesicles against K562 (C) and B16 (D) cells after 48 h incubation under static situation by CCK-8 assay. Data are represented as mean IC$_{50}$±SD ($n = 6$). ns: no significant difference $vs.$ LIPO-DOX, **$P < 0.01$, ***$P < 0.001$, ****$P < 0.0001$.

3.5.2. Antitumor effect in tumor metastasis models

As shown in Fig. 6A, mice were divided into two groups: early-treatment group and late-treatment group, representing the dynamic tumor cell model and the static cell model, respectively. Metastasis nodules on lungs were observed at the end of each experiment. The body weight change caused by different lipid vesicles showed no significant difference in both early-treatment group and late-treatment group (Supporting Information Fig. S9). Detected by metastasis nodule number, dual-targeting lipid vesicles showed a better therapeutic effect than single-targeting lipid vesicles in each group. However, the difference between dual-targeting lipid vesicles and control in early-treatment group was more significant than that in late-treatment group (Fig. 6B). Direct observation of the lung organs is shown in Fig. 6C. As for H&E staining analysis, the tumor cell masses were the least in dual-targeting lipid vesicles (Fig. 6D).

3.5.3. Biodistribution of targeted lipid vesicles

Firstly, we used healthy BALB/c nu/nu mice to investigate the in $vivo$ distribution of different lipid vesicles. Compared with free DiR, DiR-loaded lipid vesicles showed better ability of whole body distribution (Supporting Information Fig. S10A). The ex $vivo$ fluorescence imaging of organs displayed that free DiR was more easy to accumulate in lung, liver and spleen (Fig. S10B). All the lipid vesicles had a long circulating effect compared to free DiR group (Fig. S10C).

We further studied the organization distribution of lipid vesicles on leukemia mice models. As seen in Fig. 7A and C, the whole body distribution and long circulating effect of lipid

vesicles in leukemia mice were the same with that in heathy mice. As for ex $vivo$ fluorescence images, in spite of the distribution in liver and spleen, every kind of lipid vesicle was found in leg bones (Fig. 7B).

3.6. Co-localization of targeted lipid vesicles with nucleuses or lysosomes

As shown in Fig. 8A, LIPO-DOX, 50 R-LIPO-DOX, 10D-LIPO-DOX and 50R10D-LIPO-DOX mostly accumulated in lysosomes and some in nuclei after incubation for 30 min. Typically, the co-localization coefficient of 50R10D-LIPO-DOX with lysosomes and nuclei was 0.888 and 0.537, respectively, which was higher than that of other lipid vesicles (Fig. 8B−C).

3.7. Endocytosis pathways of targeted lipid vesicles

According to previous studies, chlorpromazine can inhibit the transfer from the plasma membrane to intracellular vesicles by suppressing clathrin-coated pit formation[33]. Cytochalasin is known to depolymerize the actin cytoskeleton and causes clustering of caveolae[34]. EIPA is an inhibitor of macropinosome formation via blocking Na$^+$/H$^+$ exchanger[35]. Filipin depresses the caveolae/lipid raft-mediated endocytosis[36]. Mβ-CD is an inhibitor of cholesterol-dependent endocytic process[37]. Ly-294,002 suppresses phagolysosome fusion by phosphoinositide 3-kinase signaling pathway[38]. Firstly, all the lipid vesicles and inhibitors used in this experiment showed no significant cytotoxicity on Jurkat cell line (Supporting Information Fig. S8). Then among all
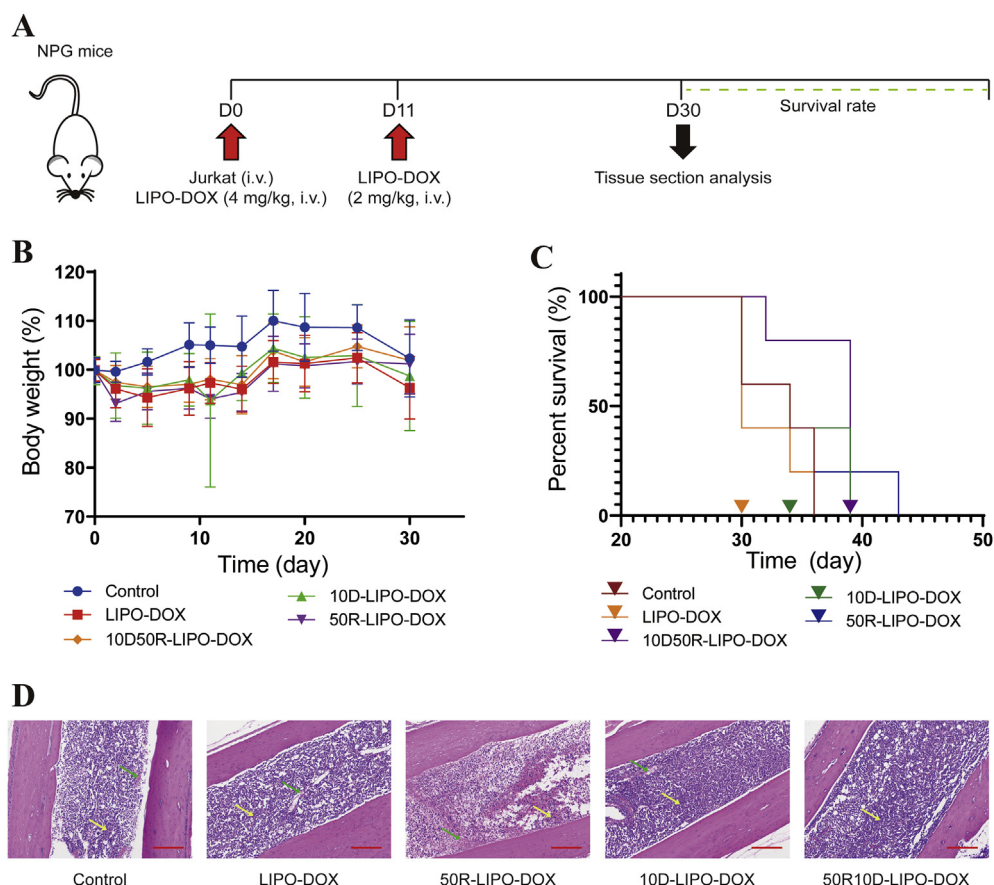
Figure 5 (A) Experimental procedure for pharmacological experiment on leukemia mice models. (B) Body weight changes. Body weight was considered as 100% on Day 0. Data are represented as mean body weight±SD ($n = 5$). (C) Survival rate of leukemia mice models receiving different treatments. Triangles represent median survival. Paralysis and mice that lost more than 25% of their body weight were considered as dead. $n = 5$. (D) H&E staining images of the leg bone tissues. Yellow arrows point to tumor cell masses and green arrows point to necrotic bone marrow cells. Scale bars are 200 μm $n = 4$.

inhibitors as seen in Fig. 8D−G, mβ-CD obviously decreased the cellular uptake of different lipid vesicles, revealing a caveolae-related uptake mechanism. While, chlorpromazine only decreased the uptake of 10D-LIPO-C6, likely owing to the involvement of clathrin. Namely, the endocytosis pathway of 10D-LIPO-C6 might be different from the other lipid vesicles.

4. Discussion

It was found in our study, all the DT4 modified lipid vesicles were easy to precipitate in $(NH_4)_2SO_4$ solution. It was likely that the ions in ammonium sulfate solution bound to liposomal surface due to the static electricity of DT4 molecules, so the hydration shell on the surface of lipid vesicle was destructed[39]. As a result, 10% was the highest DT4 concentration that could be used. To increase the stability of lipid vesicles, we removed the ions from the external aqueous phase of lipid vesicle suspension. Besides, it is quite difficult to directly determine the content of ligands on the nanoparticles. As most previous studies[26], the ligand added was taken as the final level of ligand in the nanoparticles. In addition, it was reported that the high percentage of ligand reduced the blood circulation time of nanomedicines[40]. Here, the fluorescence intensity−time curve of targeting nanovesicles was very similar to that of non-targeting lipid vesicles in two types of mice models

(Fig. 7 and Supporting Information Fig. S10), suggesting that our situation was somehow different from the report.

The endocytosis process of lipid vesicles can be divided into two steps: surface binding and internalization. The fast binding of DT4 with integrin αvβ3 provided a potential to increase cellular uptake, but DT4 also showed fast dissociation from such binding. So we considered the use of RGDm7 based on its "slow-binding/slow-unbinding" pattern, in order to establish a "fast-binding/slow-unbinding" targeted lipid vesicle delivery system. Theoretically speaking, there is a risk of "slow-binding/fast-unbinding", but the studies by real-time confocal microscopy proved that the optimized dual-targeting nanovesicles overall had a "fast-binding/slow-unbinding" feature (Fig. 3C and D).

Although dual-targeting lipid vesicles showed better specificity and therapy effect under *in vitro* conditions, the obvious differences were observed between the static and dynamic situation. In Fig. 3A, we found that under static situation, the uptake of 10D-LIPO-C6 and 10R10D-LIPO-C6 was even less than negative control, so we conducted another study in Fig. 3B to clarify this phenomenon. As showed in Fig. 3B, the uptake of 10D-LIPO-C6 and 10R10D-LIPO-C6 was higher than negative control under flowing conditions, so this demonstrated that the dynamic state could improve endocytosis of nanovesicles. Similar to the comparison between 50R10D-LIPO-C6 and 10R10D-LIPO-C6 in Fig. 3A, these two formulations were further compared in Fig. 4A
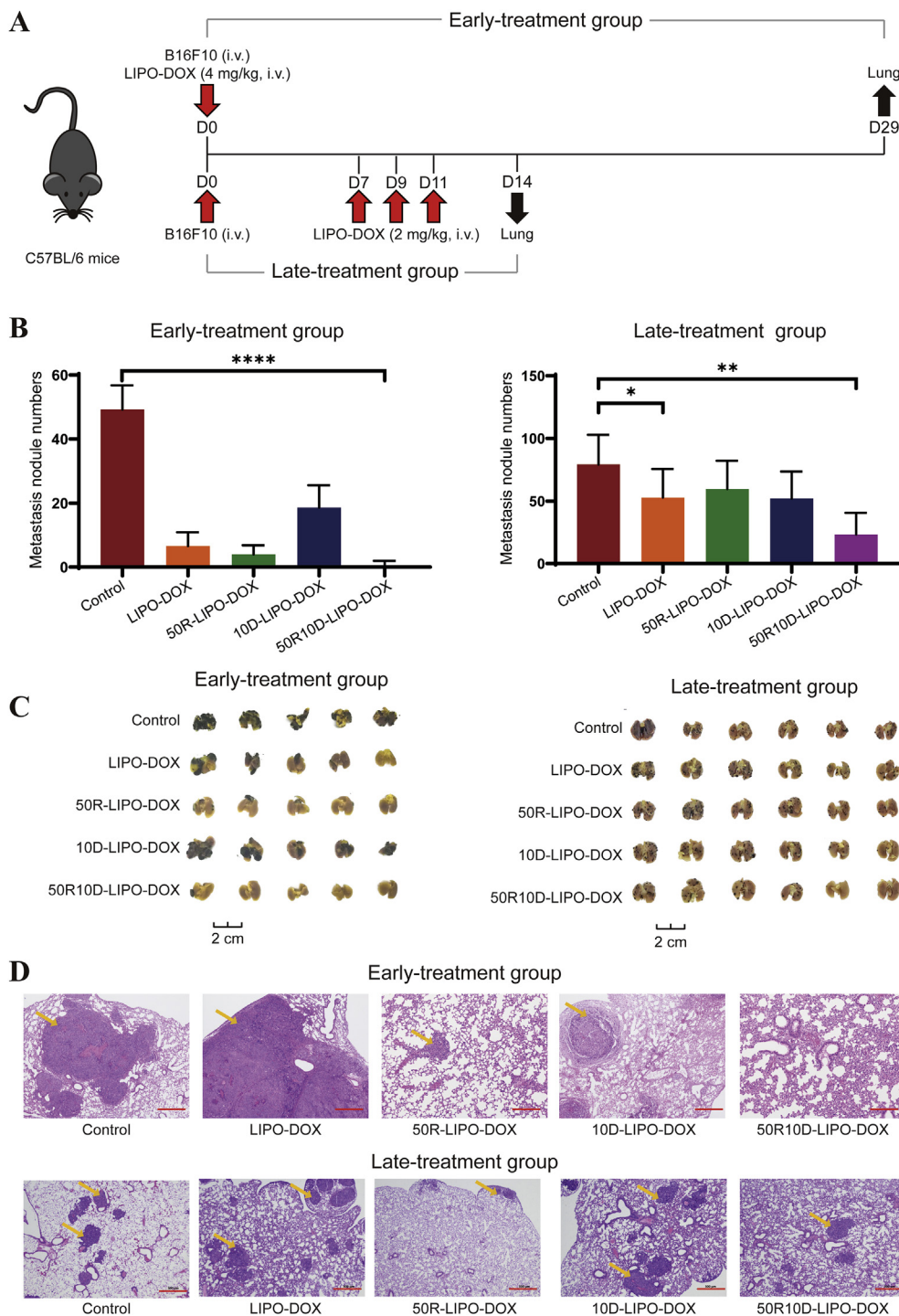
Figure 6 (A) Experimental procedure for pharmacological experiment on tumor metastasis models. (B) Number of metastatic colonies on the lung surfaces after lungs were excised at the end of the test (data represented as mean metastasis nodule numbers±SD, $n = 5$ in early-treatment group, and $n = 6$ in late-treatment group). $^{*}P < 0.05$, $^{**}P < 0.01$, $^{****}P < 0.0001$. (C) Direct observation of the lung organs. (D) H&E staining images of lung tissues. Yellow arrows point to tumor cell masses. Scale bar of 50 R-LIPO-DOX in early-treatment group is 200 μm, and the others are 500 μm.

in static and Fig. 4B in dynamic cell states. Though the increase of flowing rate decreased the cell uptake of all modified lipid vesicles compared to the control (Fig. 3B), the 50R10D-LIPO-DOX showed greatest antitumor activity under flowing state (Fig. 4A and B), so this formulation was used as the optimized one. As for *in vivo* experiments, the efficacy of dual-targeting lipid vesicles

was better when tumor cells were still circulating in blood circulatory system. Namely, the *in vitro* and *in vivo* findings were consistent.

DT4 could bind with integrin receptors, but the cellular uptake and cytotoxicity of some DT4 modified vesicles decreased in Figs. 3A and 4B. The possible reasons might include the fast

Figure 7 (A) *In vivo* fluorescence imaging of leukemia mice models treated with different lipid vesicles encapsulating DiR and control ($n = 4$) and time points post-injection. (B) *Ex vivo* fluorescence imaging of organs excited at 48 h post-injection. (C) Whole-body quantitative fluorescence intensity of leukemia mice model treated with different lipid vesicles encapsulating DiR and control. Data are represented as mean avg radiance±SD ($n = 4$) and time points post-injection. *$P < 0.05$.

dissociation rate[41,42] and efflux mechanisms[43,44] of DT4. Besides, as the RGD could interfere the function of LT4[45], we inferred that RGDm7 and DT4 might have antagonistic effects at certain condition. However, the optimized formulation of 50R10D-LIPO demonstrated high cell uptake and cytotoxicity in integrin positive cells.

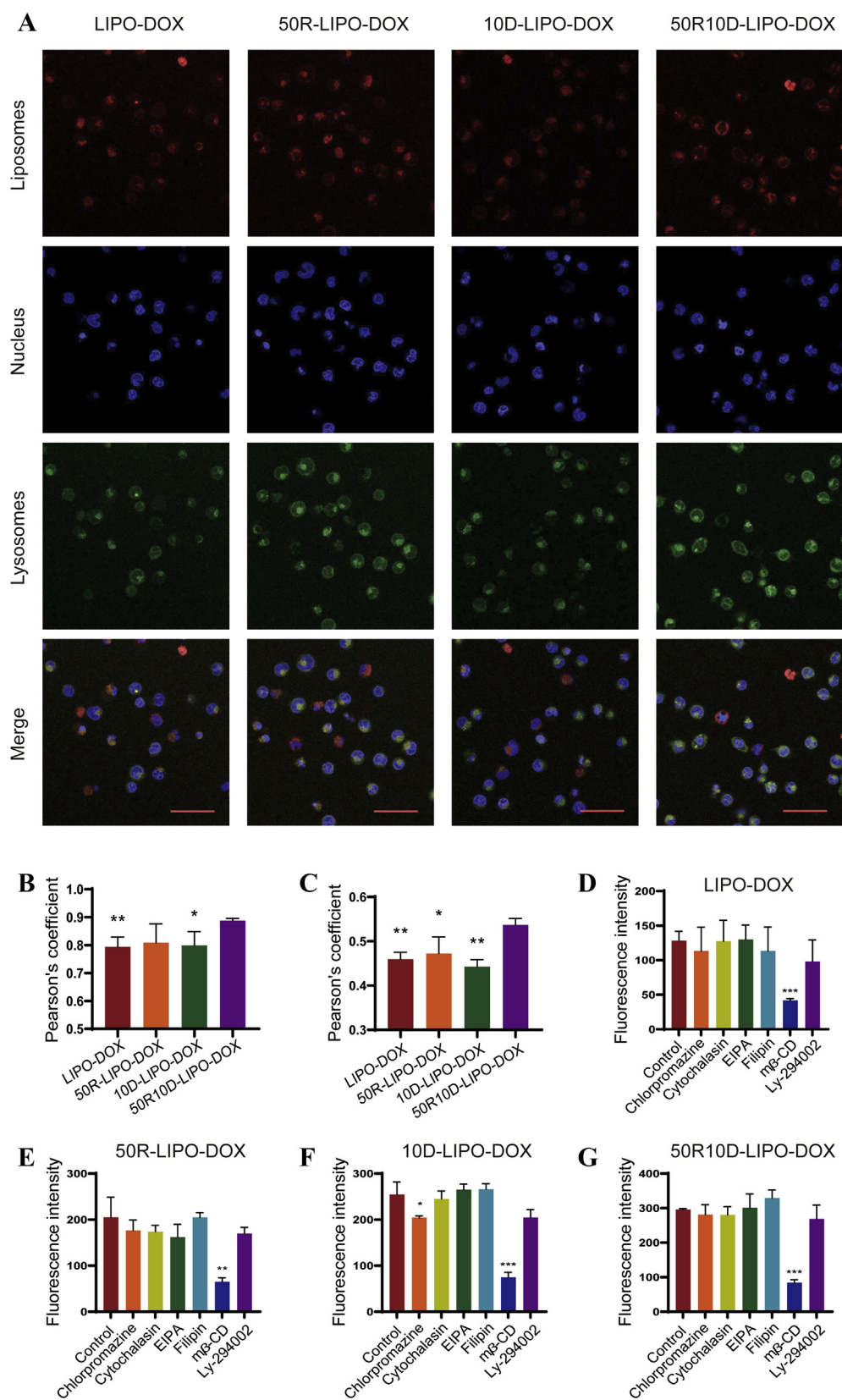Doxorubicin is a typical chemotherapy drug which reacts with DNA-associated enzymes and inserts to the DNA's double helix[46]. Based on such DNA-related mechanism, its cytotoxicity can enhance if the accumulation of DOX in nucleus increases. It is reported that the nuclear-targeting DT4 helps lipid vesicles bind to the cell nucleus and release DOX after endocytosis[22]. The increase of nuclear co-localization of dual-targeting lipid vesicles was confirmed by confocal microscopy (Fig. 8A and C). However, the nuclear co-localization of 10D-LIPO-DOX did not show a significant increase than LIPO-DOX, possibly because the total endocytosis of 10D-LIPO-DOX was not as much as dual-targeting lipid vesicles.

Injection of tumor cell suspension from tail vein was widely used to establish orthotopic leukemia model. For instance, Deng et al.[47] injected C1498 cells into C57BL/6 mice for the

development of leukemic disease[47], and Usman et al.[48] injected MOLM13 cells into the tail vein of NSG mice[48]. Here, we intravenously injected Jurket cells into NPG mice for the first time and the model development was mainly confirmed by tissue section analysis of leg bone. Spine curvature, tumor mass in bone marrow and bone marrow necrosis indicated the success of modeling. The paralysis of leukemic mice was also noticed and it might be due to the compression of leukemic cells in spine and the destruction of vertebra[49].

In our previous experiments, we observed that NPG mice were sensitive to DOX, and higher DOX dose had obvious toxicity to NPG mice. Considering the relatively high release rate of LIPO-DOX, the toxicity of DOX might lead to a shorter survival time of mice treated with LIPO-DOX. In addition, as many studies have proved that the antitumor effect of DOX liposomes *in vivo* is significantly better than free DOX, and the main goal of this study is to explore the advantages of dual-targeting nanovesicles over liposomal DOX. So, the formulation of free DOX which used less than liposomal one currently, was not used as a control here.

As for the anti-metastasis experiment, there are two treatment regimens. Because tumor cells were flowing in peripheral blood

Figure 8 (A) Confocal images of Jurkat cells after incubation with different lipid vesicles for 30 min and treated with Hoechst 33,342 and lysosome tracker for 30 min. Red represents different lipid vesicles, blue represents the nucleus and green represents lysosomes. Scale bars = 50 μm. Lysosomal (B) and nuclear (C) co-localization coefficient of different lipid vesicles. Data are represented as mean Pearson's coefficient±SD, $n = 3$. $^*P < 0.05$ vs. 50R10D-LIPO-DOX, $^{**}P < 0.01$ vs. 50R10D-LIPO-DOX. (D)−(G) Cellular uptake in Jurkat cells treated by different lipid vesicles after pre-incubation with different inhibitors by flow cytometry. Data are represented as mean fluorescence intensity±SD, $n = 3$. $^*P < 0.05$ vs. control, $^{**}P < 0.01$ vs. control.

circulatory system on the day of injection[50], dynamic tumor cell models in early-treatment group were established *in vivo* by administering lipid vesicles immediately after the inoculation of tumor cells. In late-treatment group, the first dose of lipid vesicles was not given until the 7th day after cell inoculation, so the most tumor cells located in lung and stayed static, which is typical lung metastasis model. As Fig. 6 showed, metastasis nodule number in lung was quite fewer in early-treatment group than that in late-treatment group. It seemed reasonable because the circulating tumor cells in early-treatment group might contact with lipid vesicles more directedly, leading to better anti-metastasis.

The whole-body quantitative fluorescence intensity of different lipid vesicle groups was higher than the DiR control in varying degrees (Fig. 7C), which indicated a long circulating effect of lipid vesicles due to the PEG decoration. Some studies indicated that liposomes used to treat leukemia in the bone marrow had more internalization by leukemic cells[51,52]. The general accumulating of different lipid vesicles in leg bone might be resulted from the EPR effect, the targeting to the tumor cells in bone, and the homing effect of CTCs.

The differences between the static and dynamic situation may be induced by the fluidic shear stress (FSS). Cells in flowing condition deform due to shear stress applied by the flow fluid around the cells[53]. FSS is positively related to fluid linear velocity. In this study, shaking table provided a mean fluid linear velocity of about 160 cm/min, while peristaltic pump offered a fluid linear velocity of about 500 cm/min. FSS provided by peristaltic pump was larger than that of shaking table. FSS influences the interaction between nanoparticles and cells, and also regulates specific cellular processes[54]. Previous study reported that the adhesion of ligand coated nanoparticles to cells decreased when the FSS increased[55]. That fact indicates that the fast and stable binding between tumor cells and lipid vesicles under dynamic station is particularly important. Furthermore, FSS was found to significantly increase the cytotoxicity of the ROS-generating drugs including DOX[56], which also supports our choice of drug in this study.

CTCs in peripheral blood circulatory system can induce tumor metastasis and recurrence[57], but there is currently a serious lack of investigations on the CTC-targeting nanodrugs. This study might provide new insights for establishing novel drug delivery systems to destruct CTCs and prevent tumor metastasis.

5. Conclusions

We found that RGDm7 and DT4 had different binding behaviors with αvβ3. A "fast-binding/slow-unbinding" dual-targeting lipid vesicle was developed by modifying both RGDm7 and DT4. Great cellular uptake and cytotoxicity abilities *in vitro* of the dual-targeting lipid vesicle were shown both in static and flowing situation. Treatment efficacy for leukemia and tumor metastasis models was highly effective. Furthermore, the potency of dual-targeting lipid vesicles in flowing situation was better than which under static condition. Dual-targeting lipid vesicle has appeared to be an efficient therapy strategy for tumor cells under flowing condition.

Acknowledgments

Author contributions

Conflicts of interest

The authors have no conflicts of interest to declare.

Appendix A.   Supporting information

Supporting data to this article can be found online at https://doi.org/10.1016/j.apsb.2020.07.012.

References

1. Joosse SA, Gorges TM, Pantel K. Biology, detection, and clinical implications of circulating tumor cells. *EMBO Mol Med* 2015;**7**:1−11.
2. Al-Attar T, Madihally SV. Recent advances in the combination delivery of drug for leukemia and other cancers. *Expet Opin Drug Deliv* 2020;**17**:213−23.
3. Poudineh M, Sargent EH, Pantel K, Kelley SO. Profiling circulating tumour cells and other biomarkers of invasive cancers. *Nat Biomed Eng* 2018;**2**:72−84.
4. Guan XM. Cancer metastases: challenges and opportunities. *Acta Pharm Sin B* 2015;**5**:402−18.
5. Prabhakar U, Maeda H, Jain RK, Sevick-Muraca EM, Zamboni W, Farokhzad OC, et al. Challenges and key considerations of the enhanced permeability and retention effect for nanomedicine drug delivery in oncology. *Canc Res* 2013;**73**:2412−7.
6. He HS, Lu Y, Qi JP, Zhu QG, Chen ZJ, Wu W. Adapting liposomes for oral drug delivery. *Acta Pharm Sin B* 2019;**9**:36−48.
7. Sun S, Zou H, Li L, Liu Q, Ding N, Zeng L, et al. CD123/CD33 dual-antibody modified liposomes effectively target acute myeloid leukemia cells and reduce antigen-negative escape. *Int J Pharm* 2019;**568**: 118518.
8. McCallion C, Peters AD, Booth A, Rees-Unwin K, Adams J, Rahi R, et al. Dual-action CXCR4-targeting liposomes in leukemia: function blocking and drug delivery. *Blood Adv* 2019;**3**:2069−81.
9. da Rosa FC, Buque Pardinho R, Schultz Moreira ME, de Souza LGT, de Moraes Flores EM, Mortari SR, et al. *In vitro* stability of arsenic trioxide-liposome encapsulates for acute promyelocytic leukemia treatment. *Leuk Res* 2019;**76**:11−4.
10. Maakaron JE, Mims AS. Daunorubicin-cytarabine liposome (CPX-351) in the management of newly diagnosed secondary AML: a new twist on an old cocktail. *Best Pract Res Clin Haematol* 2019;**32**: 127−33.
11. Lim WS, Tardi PG, Xie XW, Fan MN, Huang R, Ciofani T, et al. Schedule- and dose-dependency of CPX-351, a synergistic fixed ratio cytarabine:daunorubicin formulation, in consolidation treatment against human leukemia xenografts. *Leuk Lymphoma* 2010;**51**: 1536−42.
12. Feldman EJ, Lancet JE, Kolitz JE, Ritchie EK, Roboz GJ, List AF, et al. First-in-man study of CPX-351: a liposomal carrier containing cytarabine and daunorubicin in a fixed 5:1 molar ratio for the treatment of relapsed and refractory acute myeloid leukemia. *J Clin Oncol* 2011;**29**:979−85.
13. Chen HJ, Niu G, Wu H, Chen XY. Clinical application of radiolabeled RGD peptides for PET imaging of integrin αvβ3. *Theranostics* 2016;**6**: 78−92.

14. Koh B, Park SB, Yoon E, Yoo HM, Lee D, Heo JN, et al. AlphaV-beta3-targeted delivery of camptothecin-encapsulated carbon nanotube-cyclic RGD in 2D and 3D cancer cell culture. *J Pharmacol Sci* 2019;**108**:3704−12.

15. Fu S, Xu XD, Ma Y, Zhang SB, Zhang SF. RGD peptide-based non-viral gene delivery vectors targeting integrin αvβ3 for cancer therapy. *J Drug Target* 2019;**27**:1−11.

16. Li M, Xu HM, Wang JZ. Optimized functional and structural design of dual-target LMRAP, a bifunctional fusion protein with a 25-amino-acid antitumor peptide and GnRH Fc fragment. *Acta Pharm Sin B* 2020;**10**:262−75.

17. Park JA, Lee YJ, Lee JW, Lee KC, An GI, Kim KM, et al. Cyclic RGD peptides incorporating cycloalkanes: synthesis and evaluation as PET radiotracers for tumor imaging. *ACS Med Chem Lett* 2014;**5**:979−82.

18. Gereben B, Zavacki AM, Ribich S, Kim BW, Huang SA, Simonides WS, et al. Cellular and molecular basis of deiodinase-regulated thyroid hormone signaling. *Endocr Rev* 2008;**29**:898−938.

19. Shinderman-Maman E, Cohen K, Weingarten C, Nabriski D, Twito O, Baraf L, et al. The thyroid hormone-αvβv integrin axis in ovarian cancer: regulation of gene transcription and MAPK-dependent proliferation. *Oncogene* 2016;**35**:1977−87.

20. Bergh JJ, Lin HY, Lansing L, Mohamed SN, Davis FB, Mousa S, et al. Integrin $\alpha_v\beta_3$ contains a cell surface receptor site for thyroid hormone that is linked to activation of mitogen-activated protein kinase and induction of angiogenesis. *Endocrinology* 2005;**146**:2864−71.

21. Latham KR, Apriletti JW, Eberhardt NL, Baxter JD. Development of support matrices for affinity-chromatography of thyroid-hormone receptors. *J Biol Chem* 1981;**256**:2088−93.

22. Gorman CA, Jiang NS, Ellefson RD, Elveback LR. Comparative effectiveness of dextrothyroxine and levothyroxine in correcting hypothyroidism and lowering blood lipid-levels in hypothyroid patients. *J Clin Endocrinol Metab* 1979;**49**:1−7.

23. Li C, Wang JC, Wang YG, Gao HL, Wei G, Huang YZ, et al. Recent progress in drug delivery. *Acta Pharm Sin B* 2019;**9**:1145−62.

24. Gassner C, Lipsmeier F, Metzger P, Beck H, Schnueriger A, Regula JT, et al. Development and validation of a novel SPR-based assay principle for bispecific molecules. *J Pharmaceut Biomed Anal* 2015;**102**:144−9.

25. Wu HY, Yu MR, Miao YQ, He SF, Dai Z, Song WY, et al. Cholesterol-tuned liposomal membrane rigidity directs tumor penetration and antitumor effect. *Acta Pharm Sin B* 2019;**9**:858−70.

26. Guo Z, He B, Jin H, Zhang H, Dai W, Zhang L, et al. Targeting efficiency of RGD-modified nanocarriers with different ligand intervals in response to integrin alphavbeta3 clustering. *Biomaterials* 2014;**35**:6106−17.

27. Kibria G, Hatakeyama H, Ohga N, Hida K, Harashima H. The effect of liposomal size on the targeted delivery of doxorubicin to Integrin $\alpha_v\beta_3$-expressing tumor endothelial cells. *Biomaterials* 2013;**34**:5617−27.

28. Mayer KM, Hafner JH. Localized surface plasmon resonance sensors. *Chem Rev* 2011;**111**:3828−57.

29. Menon LG, Kuttan R, Kuttan G. Inhibition of lung metastasis in mice induced by B16F10 melanomacells by polyphenolic compounds. *Canc Lett* 1995;**95**:221−5.

30. Shi S, Zhou M, Li X, Hu M, Li C, Li M, et al. Synergistic active targeting of dually integrin alphavbeta3/CD44-targeted nanoparticles to B16F10 tumors located at different sites of mouse bodies. *J Control Release* 2016;**235**:1−13.

31. Yang S, Su J, Cao J, Zhang P, Lu J, Xie W. Establishment of a novel Chinese human lung adenocarcinoma cell line CPA-Yang1 which produces highly bone metastases in immunodeficient mice. *Zhongguo Fei Ai Za Zhi* 2009;**12**:753−9.

32. Liang B, Li N, Zhang SF, Qi AH, Feng JH, Jing WW, et al. Idarubicin-loaded methoxy poly(ethylene glycol)-*b*-poly(ʟ-lactide-*co*-glycolide) nanoparticles for enhancing cellular uptake and promoting anti-leukemia activity. *Int J Nanomed* 2019;**14**:543−56.

33. Li-Hsien Wang KG. Mis-assembly of clathrin lattices on endosomes reveals a regulatory switch for coated Pit formation. *J Cell Biol* 1993;**123**:1107−17.

34. Thomsen P, Roepstorff K, Stahlhut M, van Deurs B. Caveolae are highly immobile plasma membrane microdomains, which are not involved in constitutive endocytic trafficking. *Mol Biol Cell* 2002;**13**:238−50.

35. Fretz M, Jin J, Conibere R, Penning NA, Al-Taei S, Storm G, et al. Effects of Na^+/H^+ exchanger inhibitors on subcellular localisation of endocytic organelles and intracellular dynamics of protein trans-duction domains HIV-TAT peptide and octaarginine. *J Control Release* 2006;**116**:247−54.

36. He B, Jia Z, Du W, Yu C, Fan Y, Dai W, et al. The transport pathways of polymer nanoparticles in MDCK epithelial cells. *Biomaterials* 2013;**34**:4309−26.

37. Rodal SK, Skretting G, Garred Ø. Extraction of cholesterol with methyl-β-cyclodextrin perturbs formation of clathrin-coated endocytic vesicles. *Mol Biol Cell* 1999;**10**:961−74.

38. Hmama Z, Sendide K, Talal A, Garcia R, Dobos K, Reiner NE. Quantitative analysis of phagolysosome fusion in intact cells: inhibition by mycobacterial lipoarabinomannan and rescue by an 1α,25-dihydroxyvitamin D3-phosphoinositide 3-kinase pathway. *J Cell Sci* 2004;**117**:2131−40.

39. Minami H, Inoue T. Aggregation of dipalmitoylphosphatidylcholine vesicles induced by some metal ions with high activity for hydrolysis. *Langmuir* 1999;**15**:6643−51.

40. Xiao W, Gao H. The impact of protein corona on the behavior and targeting capability of nanoparticle-based delivery system. *Int J Pharm* 2018;**552**:328−39.

41. Tolmachev V, Tran TA, Rosik D, Sjoberg A, Abrahmsen L, Orlova A. Tumor targeting using affibody molecules: interplay of affinity, target expression level, and binding site composition. *J Nucl Med* 2012;**53**:953−60.

42. Ren YC, Mu Y, Jiang L, Yu H, Yang SM, Zhang Y, et al. Multi-functional TK-VLPs nanocarrier for tumor-targeted delivery. *Int J Pharm* 2016;**502**:249−57.

43. Mitchell AM, Tom M, Mortimer RH. Thyroid hormone export from cells: contribution of P-glycoprotein. *J Endocrinol* 2005;**185**:93−8.

44. Friesema ECH, Jansen J, Jachtenberg JW, Visser WE, Kester MHA, Visser TJ. Effective cellular uptake and efflux of thyroid hormone by human monocarboxylate transporter 10. *Mol Endocrinol* 2008;**22**:1357−69.

45. Cheng SY, Leonard JL, Davis PJ. Molecular aspects of thyroid hormone actions. *Endocr Rev* 2010;**31**:139−70.

46. Tacar O, Sriamornsak P, Dass CR. Doxorubicin: an update on anti-cancer molecular action, toxicity and novel drug delivery systems. *J Pharm Pharmacol* 2013;**65**:157−70.

47. Deng R, Shen N, Yang Y, Yu HL, Xu SP, Yang YW, et al. Targeting epigenetic pathway with gold nanoparticles for acute myeloid leukemia therapy. *Biomaterials* 2018;**167**:80−90.

48. Usman WM, Pham TC, Kwok YY, Vu LT, Ma V, Peng BY, et al. Efficient RNA drug delivery using red blood cell extracellular vesicles. *Nat Commun* 2018;**9**:15.

49. Li ZJ, Chen ZX, Lu J, Cen JN, He J, Chen SN, et al. Establishment of a nude mice model of human monocytic leukemia with CNS and multiorgan extramedullary infiltration. *Eur J Haematol* 2006;**77**:128−33.

50. Minn AJ, Kang Y, Serganova I, Gupta GP, Giri DD, Doubrovin M, et al. Distinct organ-specific metastatic potential of individual breast cancer cells and primary tumors. *J Clin Invest* 2005;**115**:44−55.

51. Lim WS, Tardi PG, Dos Santos N, Xie XW, Fan MN, Liboiron BD, et al. Leukemia-selective uptake and cytotoxicity of CPX-351, a synergistic fixed-ratio cytarabine:daunorubicin formulation, in bone marrow xenografts. *Leuk Res* 2010;**34**:1214−23.

52. Kim HP, Gerhard B, Harasym TO, Mayer LD, Hogge DE. Liposomal encapsulation of a synergistic molar ratio of cytarabine and dauno-rubicin enhances selective toxicity for acute myeloid leukemia

progenitors as compared to analogous normal hematopoietic cells. *Exp Hematol* 2011;**39**:741−50.

53. Skalak R, Tozeren A, Zarda RP, Chien S. Strain energy function of red blood-cell membranes. *Biophys J* 1973;**13**:245−80.

54. Kang T, Park C, Choi JS, Cui JH, Lee BJ. Effects of shear stress on the cellular distribution of polystyrene nanoparticles in a biomimetic microfluidic system. *J Drug Deliv Sci Technol* 2016; **31**:130−6.

55. Blackwell JE, Dagia NM, Dickerson JB, Berg EL, Goetz DJ. Ligand coated nanosphere adhesion to E- and P-selectin under static and flow conditions. *Ann Biomed Eng* 2001;**29**:523−33.

56. Regmi S, Fung TS, Lim S, Luo KQ. Fluidic shear stress increases the anti-cancer effects of ROS-generating drugs in circulating tumor cells. *Breast Canc Res Treat* 2018;**172**:297−312.

57. Chaffer CL, Weinberg RA. A perspective on cancer cell metastasis. *Science* 2011;**331**:1559−64.